THE JOURNAL OF PHYSICAL CHEMISTRY A
A JOURNAL OF THE AMERICAN CHEMICAL SOCIETY

pubs.acs.org/JPCA
Article

Exploring the Copper(I)-Catalyzed Azide−Alkyne Cycloaddition: A Unified Reaction Valley Approach and Local Vibrational Mode Study

Published as part of The Journal of Physical Chemistry A special issue "John F. Stanton Memorial Issue".

Lily McKenna, Thomas More Sexton, Marek Freindorf, and Elfi Kraka*

Cite This: J. Phys. Chem. A 2026, 130, 4850−4864
Read Online

ACCESS | Metrics & More | Article Recommendations | Supporting Information

ABSTRACT: The mechanism of the copper(I)-catalyzed azide−alkyne cycloaddition (CuAAC), an adaptable, regioselective, and high-yielding click reaction, was investigated using the Unified Reaction Valley Approach (URVA) and Local Mode Analysis (LMA). The cycloaddition and ring contraction steps of catalysis via both mononuclear and dinuclear catalysts, in the form of Cu(I)-acetylides forming 1,4- and 1,5-products, were explored at the B3LYP/cc-pVTZ level of theory as well as at the CCDT(T) level. The dinuclear mechanism for 1,4-addition was found to have the lowest activation energy and was identified as the most effective catalytic pathway. With the first cycloaddition step presenting the highest energy barrier, single-point energy calculations showed that this barrier is lowest for the dinuclear catalyst, while LMA suggests that regioselectivity may arise from catalyst dissociation and stronger stabilization of the final product. URVA analysis indicated that the transition state of the first step occurs prior to any C−N bond formation, signifying that the energy barrier originates from initial electronic structural changes. These mechanistic insights provide a basis for the design of more efficient CuAAC catalysts.

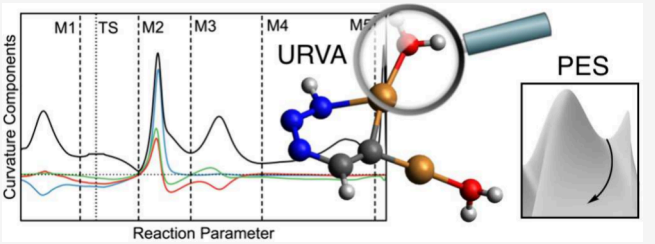

INTRODUCTION

Click chemistry, a term proposed by Kolb, Finn, and Sharpless in 2001, characterizes reactions that are adaptable, selective, and high yielding that work easily together as modular "building blocks" toward a larger synthesis.[1] Since its introduction, click chemistry has evolved from a pragmatic synthetic philosophy into a broader framework for reaction design, emphasizing orthogonality, robustness, and predictable reactivity across chemical, biological, and materials contexts. The quintessential example of a click chemistry reaction is the Copper(I)-Catalyzed Azide−Alkyne Cycloaddition (CuAAC), discovered concurrently by the Sharpless−Fokin and Meldal groups in 2002,[2,3] in which a terminal alkyne reacts with an azide to form a 1,4-disubstituted 1,2,3-triazole in the presence of a Cu(I) catalyst. The uncatalyzed azide−alkyne cycloaddition had been extensively studied by Huisgen in the second half of the twentieth century as a thermal 1,3-dipolar cycloaddition. However, it requires elevated temperatures and typically produces mixtures of the 1,4- and 1,5-regioisomers.[4] In contrast, Cu(I) catalysis transforms this reaction from a slow, weakly polarized, concerted process into a rapid and highly regioselective transformation that proceeds efficiently at room temperature and delivers almost exclusively the 1,4-regioisomer.[2] This dramatic change in reactivity and selectivity arises from copper coordination to the terminal alkyne, which lowers the activation barrier, enforces a stepwise reaction pathway, and reorganizes the frontier orbital interactions responsible for regioselection. As a result, CuAAC has emerged as the prototypical click reaction and remains the benchmark against which other click transformations are evaluated. Beyond its synthetic convenience, CuAAC has become a model for understanding how metal catalysis can fundamentally reshape the mechanism of a classical pericyclic reaction. Modern experimental and theoretical studies place CuAAC within the broader conceptual framework of Huisgen 1,3-dipolar cycloadditions, demonstrating how metal activation transforms the cycloaddition into a highly polarized, stepwise process with a strong bias toward a single regioisomer. This understanding has informed the rational design of ligand systems, heterogeneous catalysts, and bioorthogonal variants, as well as copper-free analogues that exploit strain or electronic activation.

The mechanistic understanding of CuAAC, however, emerged more gradually and remains an area of active discussion. The first detailed mechanistic proposal, advanced by Himo et al. in 2005 on the basis of density functional theory

Received: January 26, 2026
Revised: May 28, 2026
Accepted: May 29, 2026
Published: June 16, 2026

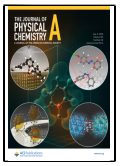

https://doi.org/10.1021/acs.jpca.6c00548
J. Phys. Chem. A 2026, 130, 4850−4864

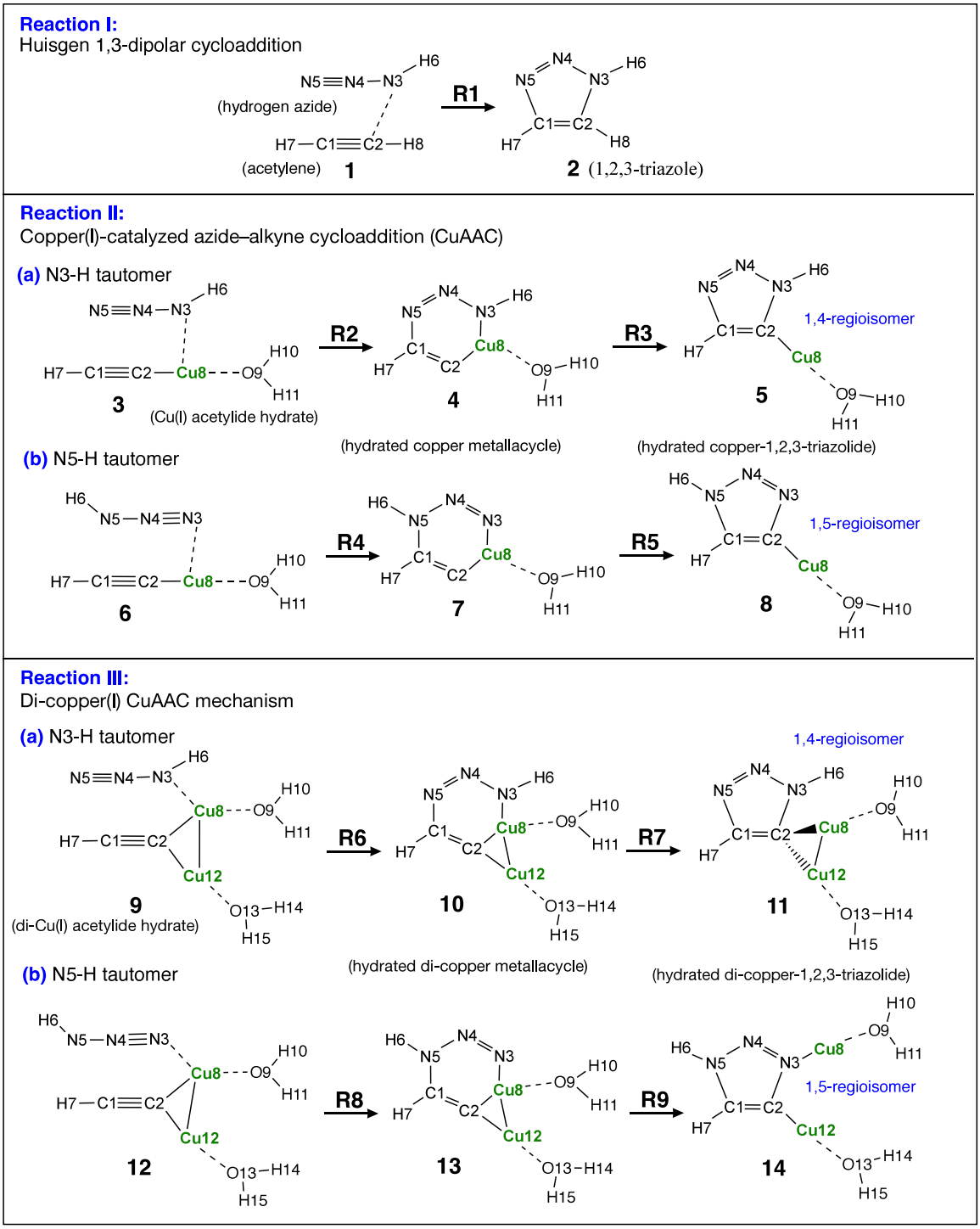

Figure 1. Schematic overview of the reaction pathways investigated in this work. **Reaction I**: uncatalyzed Huisgen 1,3-dipolar cycloaddition between azide and alkyne, yielding 1,2,3-triazole products.[74] **Reaction II**: copper(I) CuAAC proceeding through a mononuclear copper acetylide mechanism. **Reaction III**: dinuclear copper(I) CuAAC mechanism involving a di-Cu(I) acetylide species. Copper-catalyzed reactions, pathways originating from (a) the N3−H and (b) N5−H azide tautomers leading to either 1,4- or 1,5-disubstituted triazole products. Individual reactants, intermediates and products are labeled **1**−**14**. Reaction paths connecting these species on the PES are labeled **R1**−**R9**, representing distinct reaction paths on the potential energy surface. Copper hydration is modeled by an H_2O ligand on each copper atom.

(DFT) calculations, invoked a mono-copper acetylide intermediate that coordinates to the azide and promotes C−N bond formation in a stepwise fashion.[5] Subsequent kinetic experiments revealed a second-order dependence on copper concentration,[6] motivating the exploration of dicopper pathways through both experimental[7] and computational studies.[8−10] In 2013, Worrell et al. provided evidence that a second Cu(I) center is required for catalysis, supporting a dinuclear copper acetylide as a minimal active motif.[11]

In the years since, mechanistic investigations have expanded to consider the roles of higher nuclearity copper clusters containing three or four Cu(I) centers,[8,12,13] as well as the

https://doi.org/10.1021/acs.jpca.6c00548
J. Phys. Chem. A 2026, 130, 4850−4864

influence of the ligand environment, substrate electronics, and catalyst speciation on the operative reaction pathway.[14−17] These findings suggest that CuAAC may not proceed through a single rigid mechanism, but rather through a mechanistic manifold in which dinuclear intermediates are often proposed to dominate under many conditions, while alternative pathways may become accessible depending on catalyst structure and reaction environment. Nevertheless, a widely discussed mechanistic picture is the stepwise dinuclear Cu(I) mechanism proposed by Worrell et al., in which a di-Cu(I)−acetylide complex is proposed to coordinate the azide, form a six-membered metallacyclic intermediate and subsequently contract to yield the five-membered triazole product. Despite the extensive experimental and computational literature on the CuAAC reaction, several fundamental mechanistic questions remain unresolved. In particular, the physical origin of copper-induced regioselectivity, the distinct roles played by mono- and dinuclear copper species along the reaction coordinate, and the manner in which electronic and structural effects cooperatively shape the reaction pathway are still not completely understood. While previous theoretical studies have characterized stationary points on the potential energy surface (PES), a detailed, path-resolved analysis capable of disentangling the driving and resisting forces governing reaction progress is lacking. In order to address these open questions, we applied the Unified Reaction Valley Approach (URVA),[18,19] complemented by Local Mode Analysis (LMA)[20,21] to the uncatalyzed, mononuclear, and dinuclear CuAACs model reactions sketched in Figure 1. URVA provides a reaction-path-centered framework for comparing how copper coordination alters the topology of PES and redistributes electronic structure along the reaction coordinate, while LMA, employed at all stationary points, quantifies changes in the strengths of key bonds involved in the cyclization process.

COMPUTATIONAL METHODS

In the following a short introduction of LMA[20,21] and URVA[18,19] is given, followed by a description of the model chemistries and computer packages which were used for the calculations.

LMA

Information on the electronic structure of a molecule, in particular the strength of its bonds, is encoded in the normal vibrational modes.[22] However, these modes are generally delocalized, as pointed out by Wilson,[23] due to a coupling of the atomic movements during the vibration, which hinders the direct access to this valuable information. LMA, originally introduced by Konkoli−Cremer[20,21,24,25] provides a unique solution to this problem by extracting local vibrational modes and related local properties from the fundamental normal vibrational modes. The local vibrational modes reflect the local movements of an atomic fragment being described by an internal coordinate such as bond length, bond angle and dihedral angle,[20,21] or special coordinates such as Cremer−Pople ring puckering coordinates.[26] Over the past two decades, we have successfully applied local mode force constants to characterize the strength of covalent bonds and noncovalent interactions across the periodic table, analyzing molecular systems in the gas phase, solution and protein environment, as documented in two review articles which also provide a comprehensive overview of the underlying local vibrational mode theory.[20,21] Some more recent applications include the assessment of protein−ligand hydrogen bond strength patterns,[27] weak and strong π interactions in sandwich complexes,[28,29] a revised pK_a rule in light of local mode force constants for the characterization of cocrystals,[30,31] local vibrational mode force constants as features in drug design,[32,33] the characterization of metal−ligand and hydrogen bonding in hemoglobins,[34,35] cytochrome b5,[36] and bacterioferritins,[37] and the elucidation of actinide[18,29,38−40] and lanthanide bonding.[41−45]

According to eq 1 a local vibrational mode $\mathbf{a}_n$ is defined as

$$\mathbf{a}_n = \frac{\mathbf{K}^{-1}\mathbf{d}_n^{\dagger}}{\mathbf{d}_n\mathbf{K}^{-1}\mathbf{d}_n^{\dagger}} \tag{1}$$

where the two ingredients needed, the diagonal normal mode force constant matrix $\mathbf{K}$ in normal mode coordinates and the normal mode vectors $\mathbf{d}_n$ in internal coordinates, can be obtained from the output of vibrational frequency calculation via the Wilson GF formalism;[22,23,46] a standard procedure in modern quantum chemistry packages.[47] That means LMA can be applied with minimal computational costs after a routine quantum-chemical calculation of vibrational frequencies, optionally adding measured frequencies as input (a feature opening LMA to the experimental vibrational spectroscopists) not only to both single molecules in the gas phase, solution, or a protein but also to periodic systems and crystals.[20,21]

For each local mode $\mathbf{a}_n$, one can derive associated local force constants k_n^a describing the local vibration of the atomic fragment under consideration,

$$k_n^a = \mathbf{a}_n^{\dagger}\mathbf{K}\mathbf{a}_n = \frac{1}{\mathbf{d}_n\mathbf{K}^{-1}\mathbf{d}_n^{\dagger}} \tag{2}$$

local mode frequencies, local mode infrared intensities and other local properties.[20,48] Another important feature of LMA is the characterization of normal mode (CNM) procedure, which decomposes each normal vibrational mode into local mode contributions.[49,50] CNM has advanced the interpretation of vibrational spectra to the next level ranging from identifying which molecular fragments couple in DNA-base pairs to assessing the quality of Stark effect probes to elucidating vibronic coupling in lanthanide complexes.[42,44,51−54]

In this work we predominantly focused on local mode stretching force constants k_n^a(AB) reflecting the intrinsic strength the bond/interaction between two atoms A and B.[55] For the comparison of larger sets of k_n^a(AB) stretching force constants, the use of a relative bond strength order BSO n is more convenient. According to eq 3 both are connected according to the generalized Badger rule derived by Cremer, Kraka and co-workers,[56,57] via the following power relationship:

$$\mathrm{BSO}n = \nu(k_n^a)^w \tag{3}$$

The constants ν and w are calculated from k_n^a values of two reference compounds with known BSO n values and the requirement that for force constant of zero, the corresponding BSO n value is zero. For example, for CC bonds suitable references are ethane and ethylene with bond orders $n_1 = 1$ and $n_2 = 2$, respectively.[58] In the case of more complex bonding situations, e.g., metal−ligand bonding, guidance by Mayer bond orders[59−61] can be utilized.[62]

URVA

URVA explores the reaction complex (RC, i.e., the union of reacting molecules) along the path it traces out on the N_{vib} PES, with $N_{vib} = 3N - L$ internal coordinates ($L = 6$ for a nonlinear N-atomic RC and 5 for an N-atomic linear RC) starting from the transition state (TS) down into the reactant and product channels. The motion along the path is described by a large amplitude motion[63,64] and the so-called *reaction valley* is spanned by the $N_{vib} - 1$ vibrations perpendicular to the reaction path.[65−68] According to eq 4 the major focus of URVA is on the analysis of the reaction path curvature $\kappa(s)$ given at each path point s by[69−71]

$$\kappa(s) = \frac{\mathrm{d}^2\tilde{\mathbf{x}}(s)}{\mathrm{d}s^2} = \frac{\mathrm{d}\boldsymbol{\eta}(s)}{\mathrm{d}s} = \frac{[(\boldsymbol{\eta}(s))^{\dagger}\,\tilde{\mathbf{F}}(s)\,\boldsymbol{\eta}(s)]\boldsymbol{\eta}(s) - \tilde{\mathbf{F}}(s)\,\boldsymbol{\eta}(s)}{\|\tilde{\mathbf{g}}(s)\|} \tag{4}$$

https://doi.org/10.1021/acs.jpca.6c00548
J. Phys. Chem. A 2026, 130, 4850−4864

Table 1. Electronic Activation and Reaction Energy (E^a, E_R), Enthalpy (H^a, H_R), and Free Energy (G^a, G_R), in kcal/mol, of Reaction Paths R1−R9 from Both DFT and CCSD(T) Calculations[a]

	DFT						CCSD(T)					
Path	E^a	E_R	H^a	H_R	G^a	G_R	E^a	E_R	H^a	H_R	G^a	G_R
Reaction I												
R1	24.3	−62.7	24.3	−58.4	27.3	−53.4	25.0	−66.9	25.0	−62.6	28.0	−57.7
Reaction II												
R2	20.4	13.8	19.9	14.7	25.0	20.3	25.2	17.4	24.7	18.3	29.8	23.9
R3	1.2	−61.5	0.7	−59.3	0.9	−59.0	−1.9	−71.3	−2.4	−69.1	−2.3	−68.9
R4	26.8	13.1	26.5	14.5	29.9	18.0	30.3	17.0	30.0	−18.4	33.4	21.9
R5	0.4	−57.4	−0.2	−55.4	0.5	−54.3	−2.3	−67.0	−2.8	−65.0	−2.2	−63.9
Reaction III												
R6	10.5	2.7	10.7	3.7	11.7	6.8	17.9	10.2	18.1	11.3	19.1	14.4
R7	3.0	−48.2	3.2	−47.4	3.7	−44.8	0.5	−61.2	0.6	−60.4	1.1	−57.8
R8	11.4	−7.4	12.8	−4.1	13.3	−3.3	17.4	0.2	18.7	3.5	19.2	4.3
R9	1.9	−47.6	2.6	−45.5	2.6	−43.5	−1.5	−57.7	−0.8	−55.6	−0.9	−53.6

[a]DFT energies were taken from IRC calculations at B3LYP/cc-pVTZ level of theory, while single point energies were calculated with DLPNO-CCSD(T)/def2-TZVP theory. Thermochemical corrections of CCSD(T) energy were taken from DFT. Energetics are given relative to the last point on the IRC path in the reactant's direction.

where $\tilde{\mathbf{F}}(s)$ is the mass-weighted Hessian matrix in Cartesian coordinates at s and $\boldsymbol{\eta}(s)$ is the mass-weighted path direction, divided by the length of the mass-weighted gradient vector $\|\tilde{\mathbf{g}}(s)\|$.

Any electronic structure change, e.g., bond breaking/forming processes, but also rehybridization, charge polarization and transfer, etc. leads to distinct curvature peaks, which are directly reflected in the scalar reaction path curvature $\kappa(s) = \|\boldsymbol{\kappa}(s)\|$ in contrast to regions of minimal electronic change, which are reflected by curvature minima leading to a unique curvature pattern the so-called *fingerprint* of a reaction.[18,19] Deeper insights into the nature of a chemical event reflected by a curvature peak are obtained from the decomposition of the scalar reaction curvature into individual components,[72] including internal coordinates or curvilinear coordinates such as puckering coordinates,[26] providing a wealth of mechanistic information. We have applied URVA to a wide range of reactions, including organic reactions in the gas phase and in solution, homogeneous catalytic reactions, as well as reactions occurring in enzymes.[18,19] Recently, we have also begun to use URVA to explore reactions in interstellar space.[73]

Three mechanistic scenarios were explored in this work, summarized as the labeled **Reactions I−III** in Figure 1. **Reaction I** is the uncatalyzed Huisgen azide−alkyne cycloaddition, treated as a single elementary transformation described by reaction path **R1**. In contrast, the copper-catalyzed scenarios (**Reaction II** and **Reaction III**) were treated as two-step sequences: a first step in which a copper-containing six-membered metallacyclic intermediate is formed, followed by a second step corresponding to ring contraction to the five-membered triazole product. As depicted in Figure 1 for **Reaction II** (mononuclear CuAAC), the two-step sequence is represented by **R2** and **R3** for the N3−H tautomer channel (species **3** → **4** → **5**) and by **R4** and **R5** for the N5−H tautomer channel (species **6** → **7** → **8**). For **Reaction III** (dinuclear CuAAC), the corresponding two-step sequences are given by **R6** and **R7** for the N3−H tautomer channel (species **9** → **10** → **11**) and by **R8** and **R9** for the N5−H tautomer channel (species **12** → **13** → **14**). In all copper-catalyzed calculations, the catalyst was modeled as a copper acetylide (mononuclear or dinuclear, as appropriate), with copper hydration represented by explicit coordination of an H_2O ligand at each copper center. To enable direct comparison between the uncatalyzed and catalyzed scenarios, the smallest reactant set was used throughout: acetylene and hydrogen azide, together with explicit water ligand(s) on copper. While such a simplified model does not capture the full complexity and environmental sensitivity of CuAAC catalysis, it allows us to focus on a qualitative mechanistic picture. Consequently, the conclusions drawn here are not intended to be quantitatively predictive or universally applicable, but rather to provide general insights into the underlying reaction mechanism.

For each of the nine reaction paths, transition states (TSs) were located and optimized using the B3LYP functional[75,76] in conjunction with the cc-pVTZ basis set.[77] The corresponding reactants and products associated with each TS were identified by following the intrinsic reaction coordinate (IRC)[78] with a step size of 0.03 amu$^{1/2}$ bohr. Atomic charges along the IRC reaction pathways were evaluated using Natural Bond Orbital (NBO) analysis.[79−81] All IRC, NBO, and vibrational frequency calculations were performed consistently at the B3LYP/cc-pVTZ level of theory. Transition-state optimizations, frequency and IRC calculations were carried out using the Gaussian 16 software package.[82] Solvent effects of water were included in all DFT calculations explicitly with the aforementioned H_2O ligands and implicitly with the Polarizable Continuum Model (PCM).[83] Furthermore, the reaction energetics in the water solvent as well as in the gas phase are included in the Supporting Information. Single-point electronic energies were subsequently computed using the ORCA program[84] at the DLPNO-CCSD(T)/def2-TZVP level of theory[85,86] at each stationary point, using the first and last points of the IRC calculations as the reactants and products. Thermochemical corrections to the electronic energies at the DLPNO-CCSD(T) level were taken from the corresponding B3LYP/cc-pVTZ calculations. For URVA, the pURVA program[87] was used, and for LMA, the LModeA software.[88] In addition, energy densities were evaluated within the framework of the Quantum Theory of Atoms in Molecules (QTAIM)[89−91] using the AIMALL software package.[92] Bond critical points were characterized according to the Cremer−Kraka criterion, where negative energy density values indicate covalent bonding interactions, while positive values correspond to predominantly electrostatic interactions.[93] The BSO was calculated relative to CH_3NH_2, CH_2NH, CH_3Cu, and CH_2Ni. The NBO analysis was performed with the NBO7 package.[94]

Empirical dispersion corrections (e.g., Grimme D3/D4) were not included in this study due to the methodological requirements of the URVA approach. URVA relies on highly accurate and numerically stable IRC calculations. In our tests, the inclusion of empirical Grimme-type dispersion corrections introduced numerical instabilities along the IRC, leading to nonsmooth reaction curvature profiles, which compromise the reliability of the analysis. Therefore, to ensure a smooth and consistent reaction path, all calculations were performed without dispersion corrections. All calculations performed in this study are based on a closed-shell approach, and open-shell calculations were not explored for the dinuclear copper systems in order to maintain methodological consistency and enable a balanced comparison between mono- and dinuclear pathways within the computationally demanding URVA/IRC framework. A rigorous treatment of open-shell effects would require systematic calculations for all stationary points and full IRC paths for both systems, which is

https://doi.org/10.1021/acs.jpca.6c00548
J. Phys. Chem. A 2026, 130, 4850−4864

Table 2. For Reaction Paths R1, R2, R4, R6, and R8, Bond Length R (Å), Local Mode Force Constant k^a (mDyn/Å), Bond Strength Order BSO, Energy Density at Bond Critical Point H_p (hartree/bohr^3), and Difference in NBO Charge ΔQ (Calculated for Bonds C1−N5 and N3−Cu8 (N3−C2 for Reaction I)) Formed during the First Step

	C1−N5					N3−Cu8 (C2−N3 for **Reaction I**)				
Species	R	k^a	BSO	H_p	ΔQ	R	k^a	BSO	H_p	ΔQ
Reaction I										
(1)	4.833	0.015	0.015		0.145	3.532	0.041	0.032		0.303
TS(1,2)	2.138	0.134	0.076	−0.0010	0.164	2.135	0.199	0.102	−0.0090	0.276
(2)	1.360	5.799	1.250	−0.4623	0.171	1.348	6.718	1.394	−0.4857	0.233
Reaction II										
3	6.838	0.001	0.002		0.378	4.018	0.053	0.047		1.157
TS(3,4)	1.906	0.385	0.167	−0.0266	0.217	2.021	0.807	0.478	−0.0231	1.197
4	1.455	2.417	0.653	−0.2668	0.012	1.956	1.109	0.627	−0.0310	1.255
6	7.499	0.001	0.002		0.099	4.105	0.034	0.032		0.712
TS(6,7)	1.936	0.790	0.285	−0.0247	0.121	2.043	0.538	0.339	−0.0219	0.853
7	1.420	3.668	0.890	−0.3449	0.135	1.928	1.045	0.596	−0.0346	1.009
Reaction III										
9	3.412	0.021	0.019		0.227	2.121	0.435	0.283	−0.0134	1.181
TS(9,10)	1.914	0.435	0.183	−0.0259	0.118	1.981	1.057	0.602	−0.0276	1.239
10	1.444	2.626	0.695	−0.2836	0.107	1.907	1.668	0.887	−0.0388	1.290
12	3.694	0.007	0.009		0.274	2.309	0.054	0.048	−0.0052	0.717
TS(12,13)	2.007	0.652	0.247	−0.0175	0.247	2.055	0.529	0.334	−0.0203	0.818
13	1.409	4.042	0.956	−0.3683	0.220	1.897	1.322	0.728	−0.0395	0.998

beyond the scope of the present study. The results obtained within the closed-shell framework provide a consistent mechanistic picture.

RESULTS AND DISCUSSION

Energetics

Table 1 details the electronic activation and reaction energy (E^a, E_R), enthalpy (H^a, H_R), and free energy (G^a, G_R), calculated with both DFT and CCSD(T), for each reaction path **R1**−**R9** explored in this study. The values of Table 1 are calculated relative to the last point on the IRC path in the reactant's direction. In the following sections of this manuscript we discuss energetics based on the results from CCSD(T) free energies rather than DFT results, unless otherwise noted. The simplified models of the reaction complexes used in our study may introduce uncertainties related to entropy/reference-state treatment, as well as the choice of functional and solvation model. Therefore, the reported barriers should be viewed as qualitative trends rather than quantitatively definitive values.

The uncatalyzed reaction path **R1** had an activation free energy (G^a) of 28.0 kcal/mol and was exergonic with an overall reaction free energy (G_R) of −57.7 kcal/mol. All the catalyzed first-step reaction paths—**R2**, **R4**, **R6**, and **R8**—were endergonic, with reaction free energies of 23.9, 21.9, 14.4, and 4.3 kcal/mol, respectively. The mononuclear reactions were more endergonic than the dinuclear reactions, and for each mechanism, the 1,4-addition was more endergonic than the 1,5-addition. The same four reactions had activation free energies of 29.8, 33.4, 19.1, and 19.2 kcal/mol, respectively. The mononuclear reactions had higher G^a values than the uncatalyzed reaction, while both the dinuclear reactions had lower G^a values. Furthermore, although the G^a of the mononuclear 1,5-addition **R4** was 3.6 kcal/mol greater than that of 1,4-addition **R2**, the gap between the G^a of dinuclear 1,5-addition **R8** and 1,4-addition **R6** was only 0.1 kcal/mol. These observations are consistent with previous studies showing that dinuclear catalysts have a lower activation energy than mononuclear catalysts,[8−10] but the closeness in activation energy between reaction paths **R6** and **R8** does not line up with the catalyzed reaction's selectivity for the 1,4-product. The products of each reaction, however, are bonded to the Cu catalysts in structurally distinct ways, and these differences may lead to a gap in energy in later steps of catalysis.

As for the second-step reaction paths, **R3**, **R5**, **R7**, and **R9**, they were all exergonic, with G_R of −68.9, −63.9, −57.8, and −53.6 kcal/mol, respectively. The 1,4-additions and mononuclear reactions had lower G_R, and thus were more exergonic, than the 1,5-additions and dinuclear reactions, respectively. Intriguingly, the activation free energies were all under 3 kcal/mol when calculated with DFT; however, when calculated with CCSD(T), all but one of the activation energies were found to be negative. This indicates that perhaps this part of the mechanism follows one concerted step, where the second reaction step is simply a downhill reaction to the final product. The two mononuclear reaction paths **R3** and **R5** had the two most negative G^a of −2.3 and −2.2 kcal/mol, respectively, while dinuclear reaction path **R9** had a less negative G^a of −0.9 kcal/mol, and reaction **R7** was the only reaction path to retain a positive G^a of 1.1 kcal/mol, and thus the only reaction path to maintain a stepwise mechanism, which has been previously noted in several computational studies.[12,15]

Although the regioselectivity of cycloaddition reactions is mainly related to their lower activation energies, we speculate that the regioselectivity of the analyzed reactions in this study may arise from a stronger stabilization of the final product. According to Table 1, the reaction free energy G_R of reaction **R7**, which corresponds to the final product of the 1,4-addition, has a value of −57.8 kcal/mol, while the reaction free energy of **R9**, representing the 1,5-addition, has a value of −53.6 kcal/mol, indicating a stronger stabilization of the final product in the 1,4-addition by about 4 kcal/mol.

Local Mode Analysis

While energetics provide a broad picture of each reaction, local mode analysis combined with energy density and NBO

https://doi.org/10.1021/acs.jpca.6c00548
J. Phys. Chem. A 2026, 130, 4850−4864

Table 3. For Reaction Paths R1, R3, R5, R7, and R9, Bond Length R, Local Mode Force Constant k^a, Bond Strength Order BSO, Energy Density at the Bond Critical Point H_p, and Difference in Charge ΔQ Calculated for Bonds C2−N3 and N3−Cu8 (C2−Cu8 for R9) during the Second Step, with Reaction Path R1 as Reference

	C2−N3					N3−Cu8 (C2−Cu8 for **13** and **14**)				
Species	R	k^a	BSO	H_p	ΔQ	R	k^a	BSO	H_p	ΔQ
Reaction I										
1	3.532	0.041	0.032		0.303					
TS(1,2)	2.135	0.199	0.102	−0.0090	0.276					
1	1.348	6.718	1.394	−0.4857	0.233					
Reaction II										
4	2.514	0.437	0.184		0.356	1.956	1.105	0.625	−0.0309	1.256
TS(4,5)	2.230	0.462	0.191		0.317	2.010	0.913	0.531	−0.0160	1.226
5	1.362	5.841	1.257	−0.4574	0.027	2.914	0.697	0.422		0.897
7	2.597	0.290	0.136		0.041	1.927	1.050	0.598	−0.0347	1.009
TS(7,8)	2.380	0.541	0.215		0.040	1.983	0.935	0.542	−0.0255	0.996
8)	1.387	4.791	1.085	−0.4156	0.022	2.909	0.617	0.380		0.868
Reaction III										
10	2.559	0.598	0.232		0.120	1.906	1.676	0.891	−0.0389	1.292
TS(10,11)	2.231	0.324	0.147		0.093	1.996	1.007	0.577	−0.0263	1.286
11	1.378	5.475	1.198	−0.4325	0.169	2.894	0.411	0.269		0.966
13	2.626	0.453	0.189		0.319	1.846	1.951	1.014	−0.0610	1.317
TS(13,14)	2.229	0.214	0.108		0.279	1.877	1.585	0.850	−0.0500	1.268
14	1.384	5.047	1.128	−0.4294	0.134	2.918	0.572	0.357		1.024

calculations was used to evaluate how selected bond strengths evolve at stationary points (reactants, transition states, and products) along the IRC.

Table 2 summarizes the variation in bond length, bond strength, covalent bond character, and atomic charge difference, via LMA, for bonds C1−N5 and N3−Cu8 (or C2−N3 for **R1**) along the uncatalyzed reaction pathway and the first step of the catalyzed reaction pathways: **R2**, **R4**, **R6**, and **R8**. Both bonds are formed during this step, except in the dinuclear catalysis, where N3 is already coordinated with Cu8. For each formation of the C1−N5 bond, the same trends occur: as the atoms get closer together, the local force constant (k^a) (and accordingly, the bond strength order) increases and the energy density (H_p) becomes more negative, so the bond becomes more covalent. The formed C1−N5 bond is stronger in the 1,5-additions, with k^a values of 3.668 and 4.042 mDyn/Å for reaction paths **R4** and **R8**, respectively, than in the 1,4-additions, with values of 2.417 and 2.626 mDyn/Å for reaction paths **R2** and **R8**, respectively. For both regioisomers, the dinuclear product had a stronger C1−N5 bond than the mononuclear product, and none of these bonds were as strong as the final C1−N5 bond from the uncatalyzed reaction. Since the final product is the same, later catalytic steps likely further strengthen both the existing and newly formed bonds in the triazole. Although the trends in the charge difference are less clear than those of k^a, by and large, the difference in charge between C1 and N5 decreased as the reaction progressed, with the exception of reaction path **R4**, where the difference in charge was initially much smaller, due to the azide's flipped conformation, and then increased to a value near those of the other reactions.

For the N3−Cu8 bond formation, as the reaction progressed, the bond length shortened, and the local force constant increased from values near 0.05 mDyn/Å (except for **R6**, with an initial force constant of 0.435 mDyn/Å) to values greater than 1 mDyn/Å. Reaction path **R6**'s product had the highest local force constant of 1.668 mDyn/Å, according to Table 3. Furthermore, the dinuclear additions led to greater k^a and stronger N3−Cu8 bonds formed, and for both the dinuclear and mononuclear catalysts, the N3−Cu8 bonds were stronger in the 1,4- than in the 1,5-regioisomers. Although the N3−Cu8 bond became more covalent as each reaction progressed, the final value between −0.03 and −0.04 hartree/bohr^3 is much less negative than that of the C1−N5 bond for each reaction path. Unlike the C1−N5 bond formation, the charge difference between Cu8 and N3 increased as their bond strengthened, with the 1,5-additions having lower charge differences than the 1,4-additions, again due to the inversion of the azide's position. Finally, for reaction path **R6**, the reaction with the lowest G^a, the C1−N5 bond is one of the weakest from all the reactions, while the N3−Cu8 bond is the strongest. As N3 is originally coordinated with Cu8, the stronger N3−Cu8 bond may stabilize the TS, while the weaker C1−N5 bond creates a less stable intermediate, leading to a lower G^a.

Table 3 describes how the bond length, bond strength, covalent bond character, and atomic charge difference of the bonds C2−N3 and N3−Cu8 (or C2−Cu8 for reaction path **R9**) changed throughout the second-step catalyzed reaction paths, **R3**, **R5**, **R7**, and **R9**, with reaction path **R1** for reference. For the formation of the second C−N bond of the triazole, the trends are not as definite as with the first. For the mononuclear reaction paths **R3** and **R5**, the bond strength increased steadily as the atoms moved closer, but there was no bond critical point and thus no corresponding energy density at the TS. However, for dinuclear reaction paths **R7** and **R9**, the local mode force constant decreased then increased as the atoms grew closer. Reaction **R3**'s product had the greatest k^a, with a value of 5.841 mDyn/Å, and in general, the 1,4-additions had stronger C2−N3 bonds than the 1,5-additions, and for both, the mononuclear reaction had a stronger bond than the dinuclear reaction. Similar to the first step, the difference in charge decreased throughout the reaction, except for reaction path **R7**, where the difference decreased then increased. Finally, once again, the k^a of the C2−N3 bond for the products of all the catalyzed reactions is lower than that of the uncatalyzed

https://doi.org/10.1021/acs.jpca.6c00548
J. Phys. Chem. A 2026, 130, 4850−4864

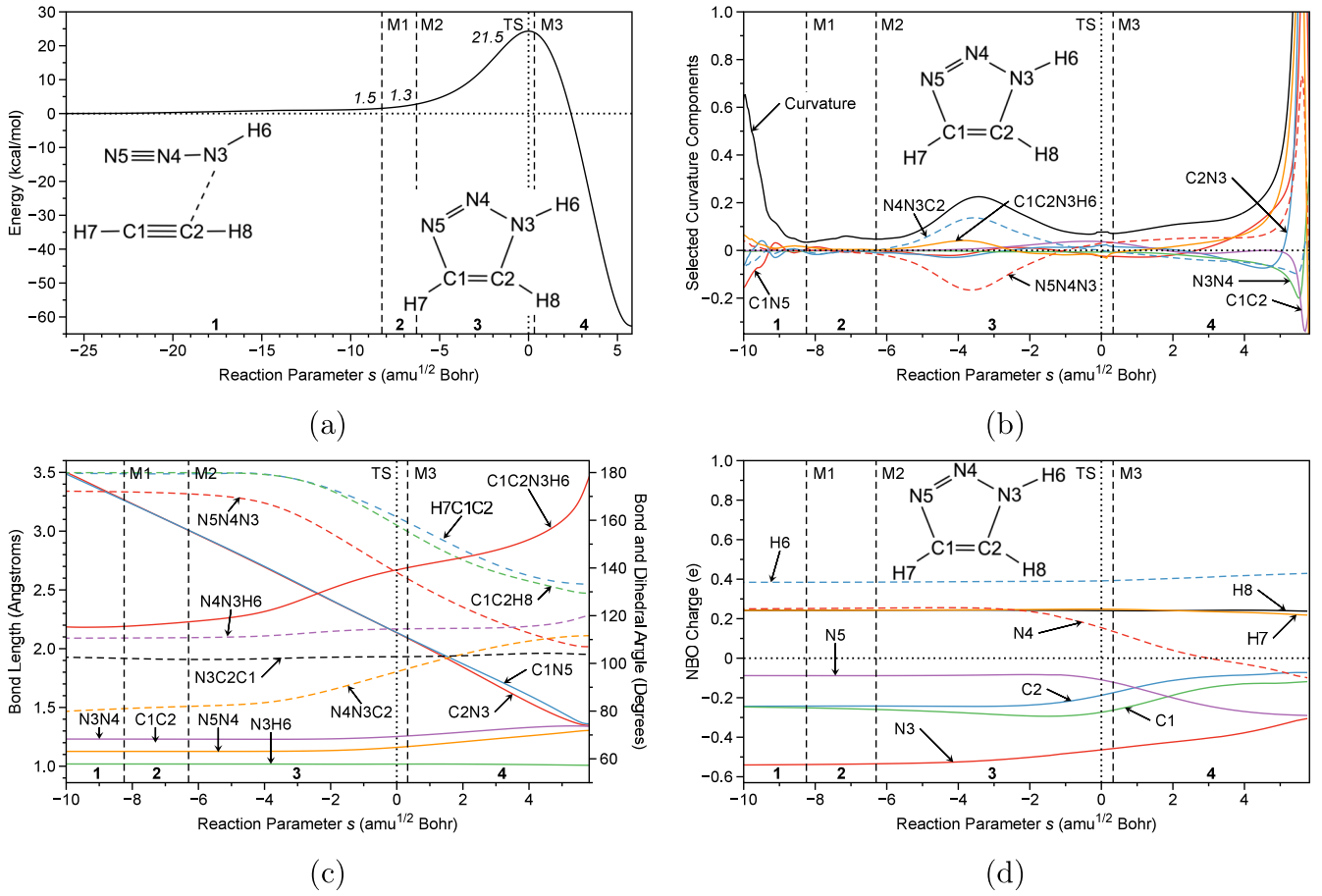

Figure 2. Plots illustrating (a) reaction energy, (b) decomposition of the reaction curvature into internal coordinates, (c) bond lengths and angles, and (d) NBO atomic charge vs reaction parameter for reaction path **R1** from URVA analysis. The bold numbers along the bottom of each figure denote the reaction phases, bounded by the minima indicated by dashed vertical lines.

reaction, suggesting that the removal of the catalyst to form the triazole in later steps will strengthen the entire ring's bonds.

During the breaking of the N3−Cu8 bond (or the C2−Cu8 bond for reaction path **R9**), the value of k^a decreases as the atoms separate, as expected. In a reversal of the first step, the charge difference between the atoms also decreased as the reaction proceeded. As H_p at the bond critical point decreases from reactants to the TS, the bond becomes less covalent. In the products, no bond critical point is observed between the two atoms. Of the three reactions where the N3−Cu8 bond breaks, reaction path **R7** had the greatest initial k^a, with a value of 1.676 mDyn/Å, while the reaction paths **R3** and **R5** had initial values of 1.105 and 1.050 mDyn/Å, respectively. Since reaction path **R7** also had the greatest (and only non-negative) G^a of the three, reaction path **R7**'s stronger N3−Cu8 bond may have contributed to the initial energy required. For reaction **R9**, the C2−Cu8 bond is stronger than in the other reactions (k^a = 1.951 mDyn/Å), yet G^a remains negative, likely reflecting its distinct mechanism.

Finally, returning to the issue of regioselectivity, according to our calculations of the chemical bonds between the Cu atom of the catalyst and the final reaction product, the local mode force constant of the C2−Cu8 and C2−Cu12 bonds of the product in reaction path **R7** were 1.962 and 1.963 mDyn/Å for the 1,4-addition. However, for the N3−Cu8 and C2−Cu12 bonds of the product in reaction path **R9**, the local mode force constants were 2.069 and 2.179 mDyn/Å for the 1,5-addition. Thus, the bonds between the catalyst and the product are stronger in reaction path **R9** than those in **R7**. Both Cu atoms will be removed in later catalysis steps to form the triazole, we therefore suggest that the additional energy required to break these stronger bonds may contribute to the observed preference for the 1,4-product. Moreover, according to Table 3, the strength of the C2−N3 bond in the product of reaction **R7** has a value of 5.475 mDyn/A, while in reaction **R9** it has a value of 5.047 mDyn/A, which could explain the stronger stabilization of the final product in **R7**. Additionally, in reaction **R7**, there is an additional Cu−Cu chemical bond between the metallic centers of the catalyst, with a strength of 0.458 mDyn/A (not shown in Table 3), which is not present in reaction **R9**. Therefore, we can conclude that the regioselectivity analyzed in this study may also arise from the stronger stabilization of the final product of reaction **R7**, which is a consequence of the stronger C2−N3 bond and the formation of a covalent bond between the metallic centers of the catalyst.

URVA Analysis

URVA analysis was carried out along the reaction pathway for each reaction path **R1**−**R9** to explore the reaction's mechanism, and the results are illustrated in the plots below.

Figure 2 depicts the results of URVA analysis on how the reaction energy, the curvature, the NBO atomic charge, and the molecular geometry change throughout the uncatalyzed reaction path **R1**. The reaction phases are indicated by the bold numbers along the bottom of each figure, and the energy

https://doi.org/10.1021/acs.jpca.6c00548
J. Phys. Chem. A 2026, 130, 4850−4864

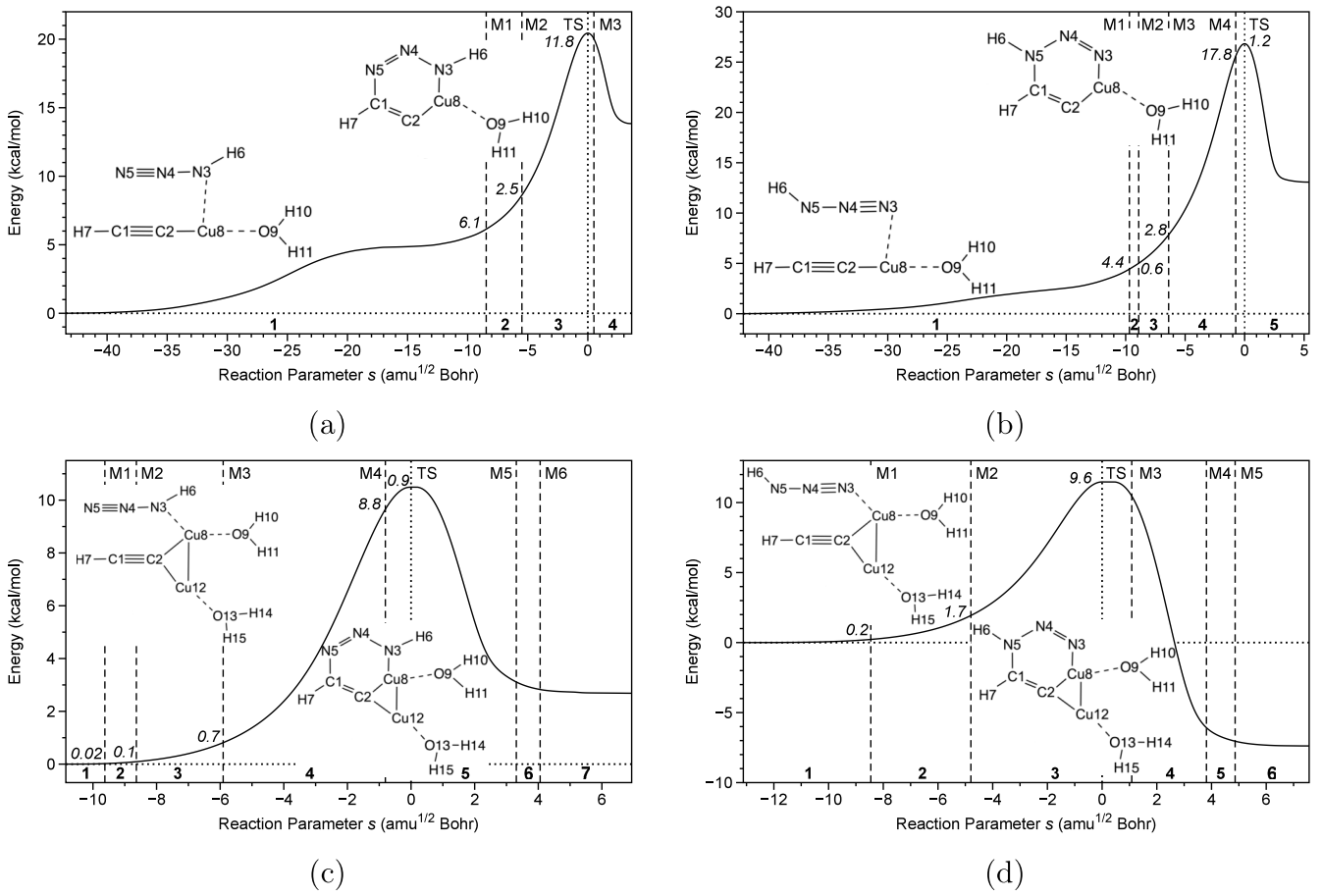

Figure 3. Energy (kcal/mol) along the reaction pathway for (a) **R2**, (b) **R4**, (c) **R6**, and (d) **R8**, calculated with IRC and URVA analysis. The italicized numbers denote the energy increase during each reaction phase until the TS.

change throughout each phase until the TS is noted by the italicized numbers in Figure 2(a). The reaction energy follows a similar path sketched by the energetics above, and reaction phase 3 led to the greatest energy increase. However, it is the curvature decomposition which best reveals the reaction's mechanism. After a period of curvature instability due to the presence of the water solvent as the molecules initially move closer, there are two major peaks in the curvature in reaction phases 3 and 4. Generally, shorter peaks in the curvature correspond to conformational changes of the reaction complex, while taller peaks correspond to substantial changes of the electronic structure like bond breakage and formation.[70] The first peak, in reaction phase 3, is shorter, and its main internal contributions come from bond angles, with positive contributions from angles where the molecules bend toward each other, like N4−N3−C2, and a negative, or resisting, contribution from existing bond angle N5−N4−N3. Furthermore, the geometry and NBO charge plots show that the first changes in bond angles and atomic charge occur at the same place along the reaction pathway. Therefore, this peak corresponds to a subtle bending in the molecular structure and the first shift of charge in the reactants from N3 to N4 and N5.

The second peak, in reaction phase 4, is higher and sharper, corresponding to bond formation. Additionally, the C1−N5 and C2−N3 bonds being formed both contribute positively to the curvature, while the existing bonds, N3−N4 and C1−C2, have a negative contribution, as they are changing from a triple to a double bond. Since the C1−N5 and C2−N3 contribute to the curvature peak at the same value of *s*, the two bond formations occur simultaneously. Furthermore, the plot of the reaction geometry in Figure 2(c) shows that the length of the C1−N5 and C2−N3 bonds stay close together throughout the reaction before leveling at the same value of *s* as the second curvature peak. Therefore, the uncatalyzed **Reaction I**'s mechanism consists of one major step of concurrent bond formation, with slight preparation beforehand in the form of bending.

To compare the mechanisms of the catalyzed reactions, Figures 3 and 4 illustrate the energy and reaction curvature decomposition, respectively, along the reaction pathway for the first-step reaction paths: **R2**, **R4**, **R6**, and **R8**. First, although all four reactions were endothermic when calculated with CCSD(T), one reaction path, **R8**, was exothermic when calculated with DFT, as shown in Figure 3. Hammond's Postulate, which has previously been applied to URVA by Cremer and Kraka,[95] proposes that, for a more exothermic reaction, the TS structure more closely resembles the products and, for an endothermic reaction, the TS structure more closely resembles the reactants.[96] In keeping with this postulate, for the more endergonic mononuclear reaction paths **R2** and **R4**, the TS is very close to the products along the reaction pathway, while for dinuclear reaction paths **R6** and **R8**, the TS is more equally positioned between the reactants and the products. Additionally, the reaction phase that corresponds to the greatest energy increase was phase 3 for

https://doi.org/10.1021/acs.jpca.6c00548
J. Phys. Chem. A 2026, 130, 4850−4864

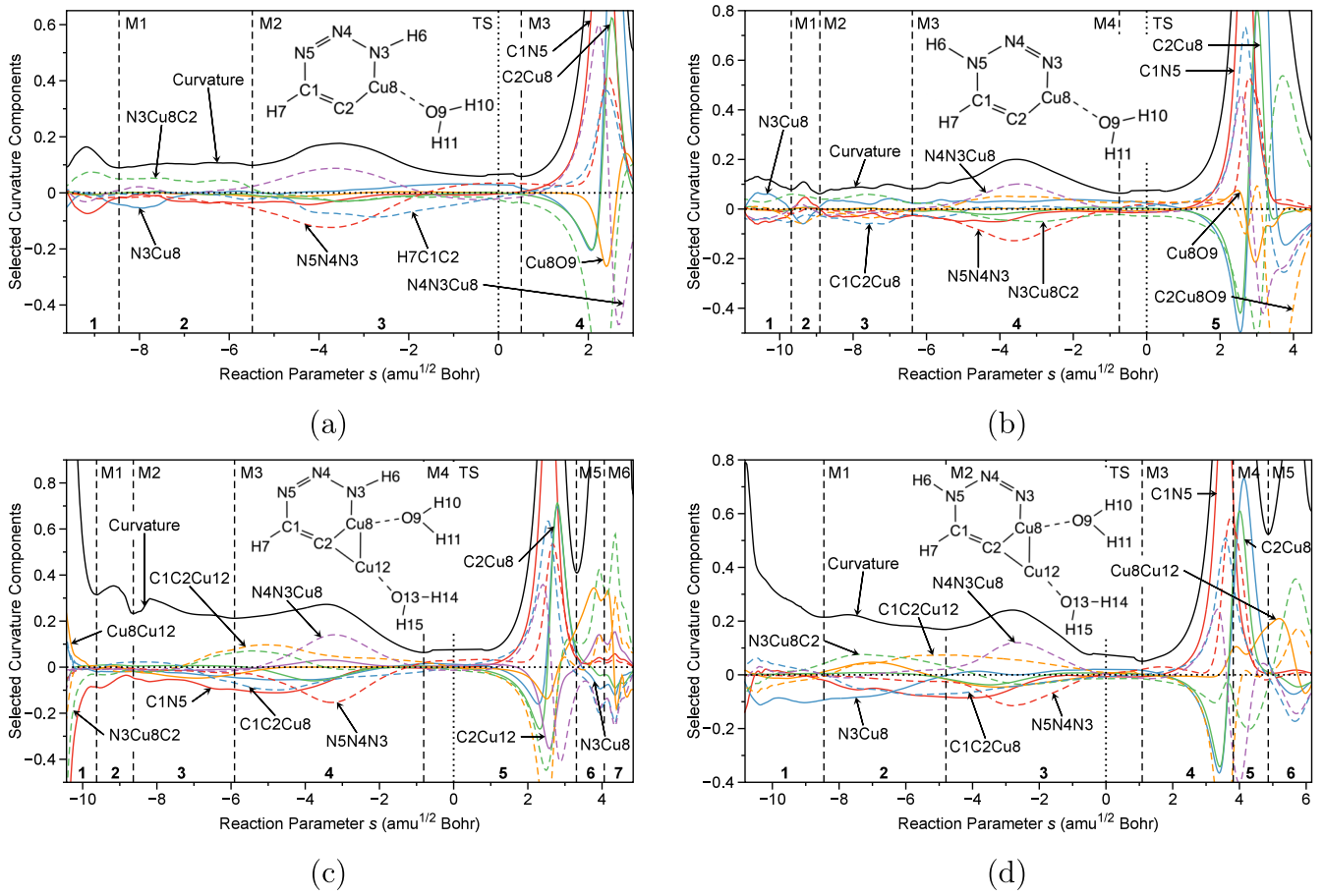

Figure 4. Decomposition of the reaction curvature into internal coordinates for (a) **R2**, (b) **R4**, (c) **R6**, and (d) **R8**, from URVA analysis. The bold numbers along the bottom of each figure denote the reaction phases.

reaction paths **R2** and **R8** and phase 4 for reaction paths **R4** and **R6**.

As for the reaction curvature, the overall structure of the first step for each reaction is similar to that of the uncatalyzed reaction: initial curvature instability, followed by a soft peak and then a sharp peak right before the products are formed, according to Figure 4. For both dinuclear reactions, the first peak is longer and flatter than those of the mononuclear and uncatalyzed reactions, and there is an additional sharp peak just after the second. Looking to the internal coordinates contributing to each peak, the first shorter peak (in reaction phase 3 for reaction paths **R2** and **R8** and reaction phase 4 for reaction paths **R4** and **R6**) has the same contributions as the uncatalyzed reaction, with positive contributions from angles like N4−N3−Cu8 and negative contributions from existing angles like N5−N4−N3 and C1−C2−Cu8. Once again, there is an initial bending and electronic structure change before the bond formation.

With the second peak (in reaction phase 4 for reaction path **R2**, reaction phase 5 for reaction paths **R4** and **R6**, and reaction phases 4 and 5 for reaction path **R8**), the positive contributions include the C1−N5 and N3−Cu8 bonds, after some initial resistance. Although both bonds contribute positively to the reaction curvature, the N3−Cu8 contribution is slight offset from the C1−N5 contribution, suggesting that the C1−N5 bond forms first causing the N3−Cu8 bond to form right after. As for the dinuclear reactions' third, sharp peak (in reaction phases 6 and 7 for reaction path **R6** and reaction phase 6 for reaction path **R8**), the contributions once again arise from coordinates that correspond to bending, specifically the N3−Cu8−C2 angle and the C1−C2−C12 angle, as well as mostly positive contributions from the Cu8−Cu12 bond. Therefore, this third peak seems to correspond to the two Cu atoms shifting into position after the 6-membered ring is formed. Since these sharp peaks occur after the TS in each reaction, the formation of the C1−N5 and N3−Cu8 bonds does not contribute to the activation energy. Instead, only the initial bending and electronic reorganization associated with the first peak contributes, corresponding to the phase with the greatest energy increase in all four reactions. For that first peak in the dinuclear reactions, the supporting contribution from the N4−N3−Cu8 angle was greater than that of the mononuclear reactions and of the analogous N4−N3−C2 angle in the uncatalyzed **Reaction I**. Furthermore, there were additional components contributing positively to the reaction curvature, like the C1−C2−Cu12 angle and the N3−Cu8−C2 angle. The increase in supporting contributions in this initial step may correspond to the lowered G^a for the dinuclear reactions. The mechanism of the first-step reaction paths follows that of the uncatalyzed reaction pretty closely, with the exception of the separation between the two bond formations.

The second step reaction paths, however, take a different path. Figures 5 and 6 show the energy and reaction curvature, respectively, along the reaction pathway for the second step reaction paths, **R3**, **R5**, **R7**, and **R9**. As mentioned above, each

https://doi.org/10.1021/acs.jpca.6c00548
J. Phys. Chem. A 2026, 130, 4850−4864

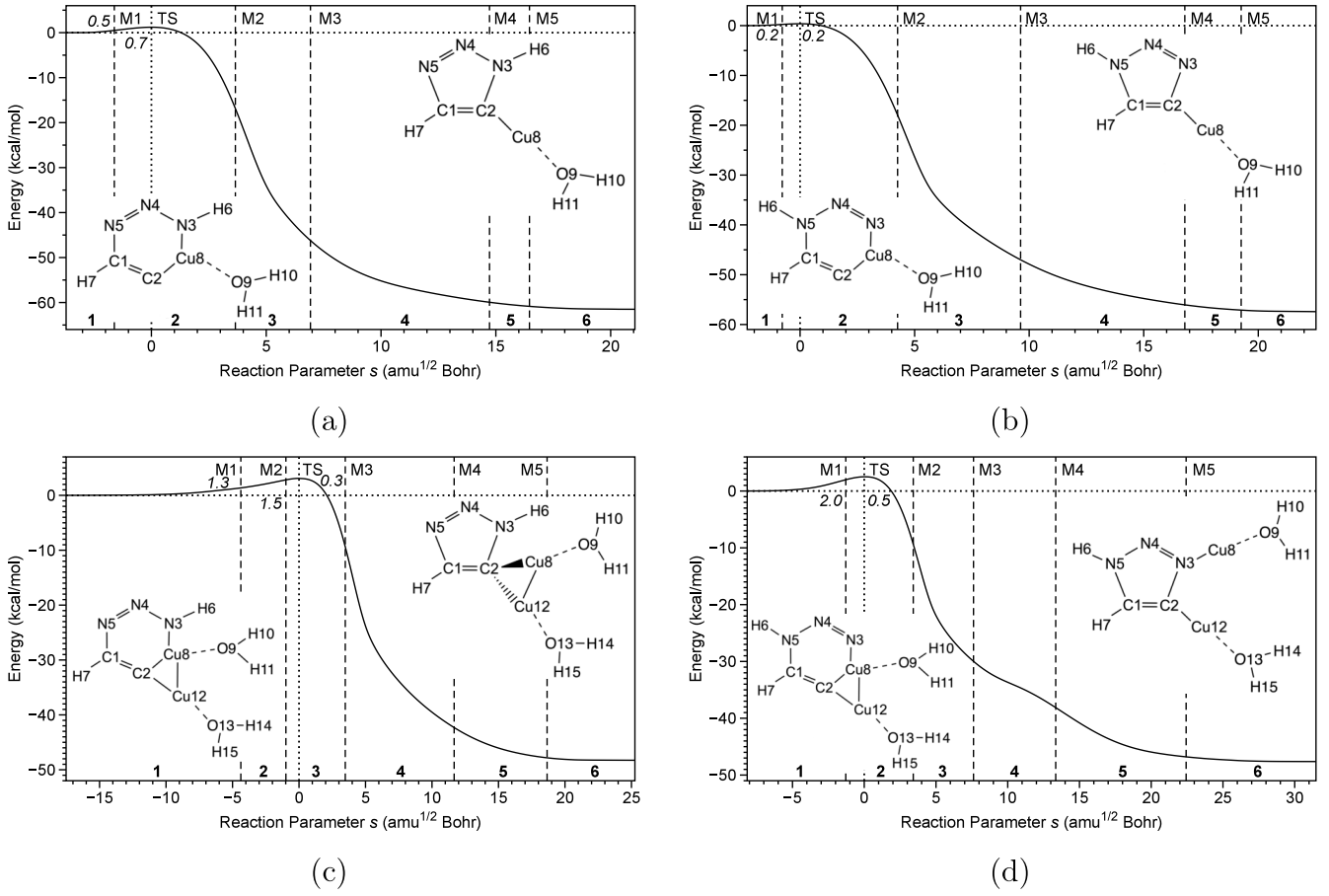

Figure 5. Energy (kcal/mol) along the reaction pathway for (a) **R3**, (b) **R5**, (c) **R7**, and (d) **R9**, calculated with IRC and URVA analysis. The italicized numbers denote the energy increase during each reaction phase until the TS.

reaction is exergonic with a very small G^a when calculated with DFT, according to Figure 5. Furthermore, note that the TS is much closer to the reactants than the products along the reaction pathway for all the reactions, except for reaction path **R7**, where the TS is closer to the middle. Once again, following Hammond's postulate, the more exergonic reactions have earlier transition states, while the less exergonic reactions' transition states occur further along the reaction pathway.

As for the reaction mechanisms, in general, each reaction's curvature had around 3 major peaks: a shorter peak, followed by a sharp peak, followed by a second shorter peak. For the first peak (in reaction phase 2 for reaction paths **R3** and **R5**, reaction phases 2 and 3 for reaction path **R7**, and reaction phases 1 and 2 for reaction path **R9**), the positive and negative components remained generally consistent between the four reactions, with supporting contributions from angles including C1−C2−Cu8 and C2−Cu8−O9, and resisting contributions from bonds like C2−N3 and N3−Cu8. Similar to the first mechanism, this first bump in the curvature represents the molecular bending into the TS, bringing C2 and N3 closer together to prepare for bond formation. Reaction path **R7** had greater resistive contributions from components like C2−N3 and N3−Cu8−C2. The TS of reaction path **R7** was the only significantly nonplanar TS, and the existing bond angles resist the twisting of the two Cu atoms out of the plane. This greater resistance and bending may contribute to reaction path **R7** being the only second step reaction that did not have a negative G^a, and thus, the only nonconcerted mechanism based on the CCSD(T) method.

The second, sharp peak (in reaction phase 3 for reaction paths **R3**, **R5** and **R9** and reaction phase 4 for reaction path **R7**) corresponds to the C2−N3 bond formation, with a large positive contribution from the C2−N3 component during each reaction. There is also a simultaneous and significant, but smaller, contribution from the N3−Cu8 bond in each reaction (as well as the analogous C2−Cu8 bond in reaction path **R9**), signifying the concurrent breaking of the Cu bond; however, the smaller nature of the contribution indicates that a greater molecular reorganization is required for the formation of the C2−N3 bond. For the final, shorter peak (in reaction phase 4 for reaction paths **R3** and **R5** and reaction phase 5 for reaction path **R7**), the C2−Cu8−O9 angle contributes positively during each reaction, while the N3−Cu8 bond is the greatest resistive contribution. Thus, this last peak appears to correspond to the Cu atoms and H_2O ligands shifting into place after the 5-membered ring has been formed. Additionally, reaction path **R9** has two slightly taller peaks in reaction phases 4 and 5 in the place of the one shorter bump, where the resistive contribution from N3−Cu8 and the positive contribution from C2−Cu12−O13 are split between the first and second peaks, respectively. The sharper, positive contribution of the Cu8−Cu12 bond as the Cu8 and Cu12 atoms move apart indicates that this first bump corresponds to the breaking of the Cu8−Cu12 bond, while the second is a

https://doi.org/10.1021/acs.jpca.6c00548
J. Phys. Chem. A 2026, 130, 4850−4864

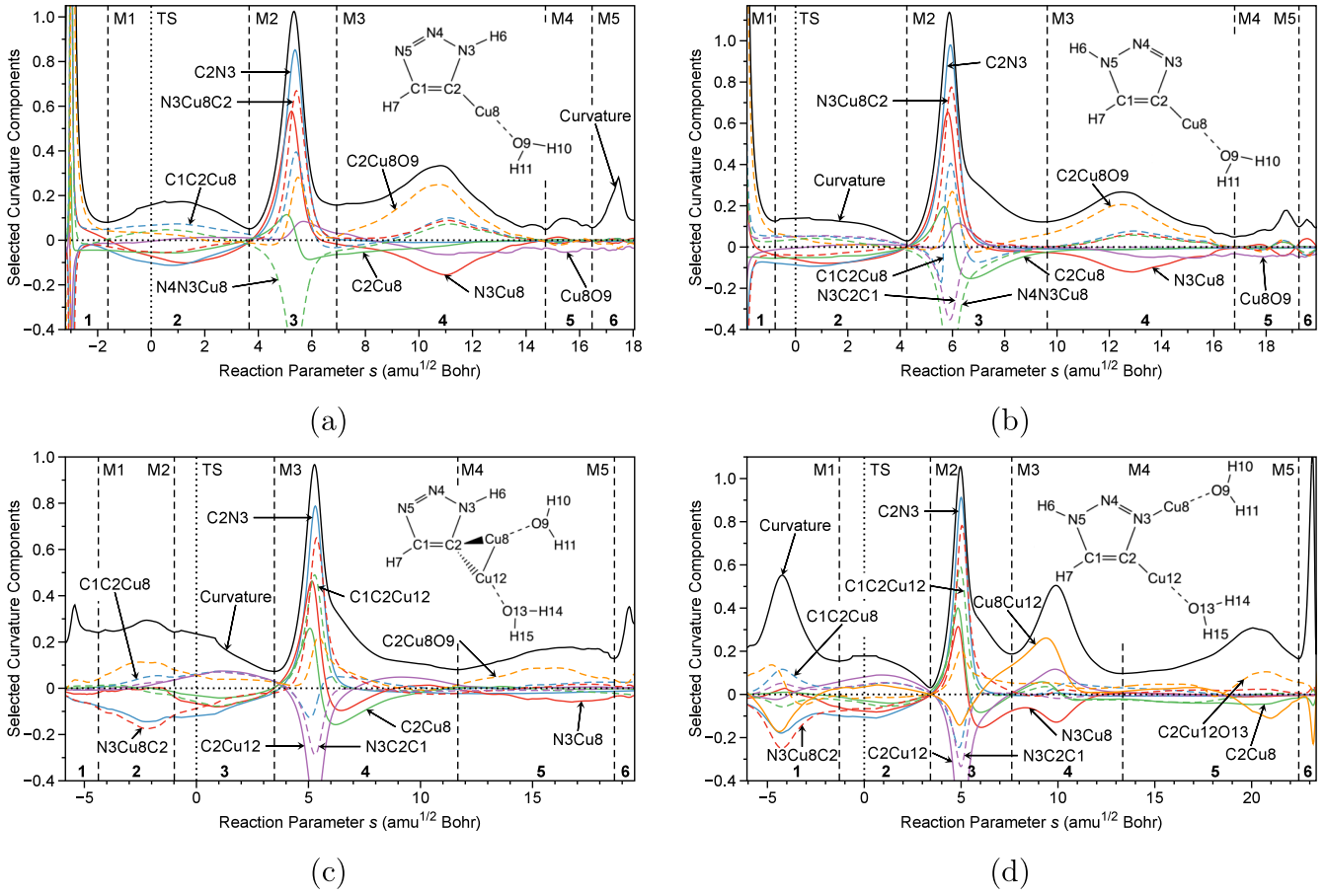

Figure 6. Decomposition of the reaction curvature into internal coordinates for (a) **R3**, (b) **R5**, (c) **R7**, and (d) **R9**, from URVA analysis. The bold numbers along the bottom denote the reaction phases.

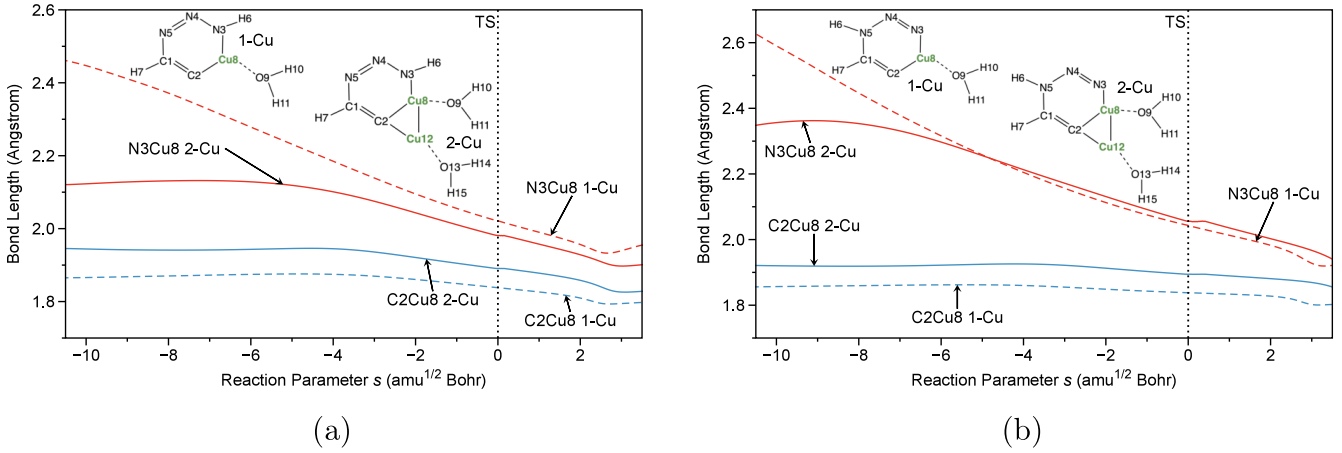

Figure 7. (a) Change of N3−Cu8 and C2−Cu8 bond lengths in 1,4-addition reaction **R2** involving one-Cu catalyst (broken line) and **R6** with two-Cu catalyst (solid line). (b) Change of N3−Cu8 and C2−Cu8 bond lengths in 1,5-addition reaction **R4** involving one-Cu catalyst (broken line) and **R8** two-Cu catalyst (solid line).

similar reorganization of the Cu atoms relative to the triazole after the bond formation and breaking.

Figure 7 panels (a) and (b) show changes of the N3−Cu8 and C2−Cu8 bond lengths in 1,4-addition and 1,5-addition reactions involving the one-Cu catalyst (broken line) and the two-Cu catalyst (solid line). According to Figure 7(a) the N3−Cu8 bond in reaction **R6** with the two-Cu catalyst is shorter than this bond in reaction **R2** with the one-Cu catalyst, which indicates that the N3−Cu8 bond is formed more easily in the reaction with the two-Cu catalyst than in the one-Cu catalyst, which is consistent with the smaller activation free energy G_R of reaction **R6** (19.1 kcal/mol) relative to reaction **R2** (29.8 kcal/mol). Similarly, according to Figure 7(b) the N3−Cu8 bond in **R8** with the two-Cu catalyst is shorter than in **R4** with the one-Cu catalyst at the initial phase of the reaction, which also indicates that the N3−Cu8 bond is formed more easily in

https://doi.org/10.1021/acs.jpca.6c00548
J. Phys. Chem. A 2026, 130, 4850−4864

the reaction with the two-Cu catalyst, and consequently the activation free energy G_R in reaction **R8** (19.2 kcal/mol) is smaller than in reaction **R4** (33.4 kcal/mol). These results are consistent with Figure 4(a),(c) showing that the supporting contribution of the N4−N3−Cu8 bond angle (broken purple line) to the reaction curvature in phase 4 of **R6** with the two-Cu catalyst is bigger than the contribution of this bond angle in phase 3 of **R2** with the one-Cu catalyst, and similar in reactions **R8** and **R4** according to Figure 4(b),(d). The bigger supporting contributions of the N4−N3−Cu8 bond angle in reactions **R6** and **R8** take place on the reaction path before the TS; therefore, they also could contribute to the smaller activation energies of the reactions with the two-Cu catalyst.

In this study, we used the URVA and LMA methods to analyze the mechanisms of the investigated reactions. The URVA method specifies the sequence of all chemical events occurring along the reaction paths, for example, providing details about which chemical bonds are formed or cleaved first or specifying the concerted or stepwise character of a chemical reaction. Moreover, URVA provides insight into which geometrical parameters of the reaction complex, such as bond lengths or bond angles, support or resist the electronic structure changes occurring from reactants to products. In our study, URVA confirmed the stepwise mechanism of the analyzed reactions, indicating which bond angles contribute to the activation energies. On the other hand, the LMA method delivers a quantitative measure of the strength of covalent bonds and nonbonding interactions, such as hydrogen bonds or van der Waals interactions, and in our study, LMA characterized the stronger stabilization of the final product, which could explain the reaction regioselectivity. Therefore, the URVA and LMA methods together provide deep mechanistic insight into the analysis of the investigated chemical reactions, offering valuable parameters for future catalyst modification.

CONCLUSION

In this study, two steps of two proposed catalysis mechanisms for the CuAAC, including both the 1,4- and 1,5-regioisomers, were analyzed using URVA and local mode analysis. The dinuclear mechanism for 1,4-addition (reaction paths **R6** and **R7**) was found to have the lowest activation energy and was determined to be the most effective catalysis mechanism. The CuAAC's regioselectivity via a dinuclear mechanism was proposed to arise from later steps involving the removal of the Cu catalyst that were out of the focus of this study and the stronger stabilization of the final product. While appearing as two steps when calculated with DFT, CCSD(T) single-point energy calculations revealed that each mechanism occurred as one concerted step, except for the dinuclear 1,4-addition. URVA analysis suggested that the stepwise nature stemmed from the rotation of the two-Cu catalysts before the TS. Furthermore, URVA revealed that the TS of the first step occurs before any bond formation, indicating that the activation energy arises from the initial bending and electronic structure shifting prior to the TS in every studied reaction.

In the future, open-shell calculations and a wider selection of CuAAC reactants could be explored to expand the scope of mechanistic understanding. While extrapolated from a minimal reactant model, the results of this study offer broad insight into the mechanisms of both the uncatalyzed and catalyzed reactions, possibly opening the door to the design of more efficient and effective Cu(I) catalysts for the CuAAC.

ASSOCIATED CONTENT

Supporting Information

The Supporting Information is available free of charge at https://pubs.acs.org/doi/10.1021/acs.jpca.6c00548.

Optimized geometries of each reactant, full energetics results in solution and gas phase, and a complete collection of URVA analysis plots (PDF)

AUTHOR INFORMATION

Corresponding Author

Elfi Kraka − *Department of Chemistry, Southern Methodist University, Dallas, Texas 75275, United States;* orcid.org/0000-0002-9658-5626; Email: ekraka@smu.edu

Authors

Lily McKenna − *Department of Chemistry, Harvard University, Cambridge, Massachusetts 02138, United States*

Thomas More Sexton − *Department of Chemistry, University of Mary, Bismark, North Dakota 58504, United States*

Marek Freindorf − *Department of Chemistry, Southern Methodist University, Dallas, Texas 75275, United States*

Complete contact information is available at: https://pubs.acs.org/10.1021/acs.jpca.6c00548

Notes

The authors declare no competing financial interest.

ACKNOWLEDGMENTS

This research received no external funding. We thank SMU's O'Donnell Data Science and Research Computing Institute for providing excellent computational resources.

REFERENCES

(1) Kolb, H. C.; Finn, M. G.; Sharpless, K. B. Click Chemistry: Diverse Chemical Function from a Few Good Reactions. *Angew. Chem., Int. Ed.* **2001**, *40*, 2004−2021.

(2) Rostovtsev, V. V.; Green, L. G.; Fokin, V. V.; Sharpless, K. B. A Stepwise Huisgen Cycloaddition Process: Copper(I)-Catalyzed Regioselective "Ligation" of Azides and Terminal Alkynes. *Angew. Chem., Int. Ed.* **2002**, *41*, 2596−2599.

(3) Tornøe, C. W.; Christensen, C.; Meldal, M. Peptidotriazoles on Solid Phase: [1,2,3]-Triazoles by Regiospecific Copper(I)-Catalyzed 1,3-Dipolar Cycloadditions of Terminal Alkynes to Azides. *J. Org. Chem.* **2002**, *67*, 3057−3064.

(4) Huisgen, R. 1−3-Dipolar Cycloadditions. Past and Future. *Angew. Chem., Int. Ed.* **1963**, *2*, 565−632.

(5) Himo, F.; Lovell, T.; Hilgraf, R.; Rostovtsev, V. V.; Noodleman, L.; B, S. K.; V, F. V. Copper(I)-Catalyzed Synthesis of Azoles. DFT Study Predicts Unprecedented Reactivity and Intermediates. *J. Am. Chem. Soc.* **2005**, *127*, 210−216.

(6) Rodionov, V. O.; Fokin, V. V.; Finn, M. G. Mechanism of the Ligand-Free Cu(I)-Catalyzed Azide-Alkyne Cycloaddition Reaction. *Angew. Chem., Int. Ed.* **2005**, *44*, 2210−2215.

(7) Iacobucci, C.; Reale, S.; Gal, J.-F.; De Angelis, F. Dinuclear Copper Intermediates in Copper(I)-Catalyzed Azide-Alkyne Cycloaddition Directly Observed by Electrospray Ionization Mass Spectrometry. *Angew. Chem., Int. Ed.* **2015**, *54*, 3065−3068.

(8) Straub, B. F. μ -Acetylide and μ -Alkenylidene Ligands in "Click" Triazole Syntheses. *Chem. Commun.* **2007**, 3868−3870.

(9) Ahlquist, M.; Fokin, V. V. Enhanced Reactivity of Dinuclear Copper(I) Acetylides in Dipolar Cycloadditions. *Organometallics* **2007**, *26*, 4389−4391.

(10) Cantillo, D.; Àvalos, M.; Reyes, B.; Cintas, P.; Jimènez, J. L.; Palacios, J. C. Accessing the Whole Range of CuAAC Mechanisms by DFT Calculations—On the Intermediacy of Copper Acetylides. *Org. Biomol. Chem.* **2011**, *9*, 2952−2958.
(11) Worrell, B. T.; Malik, J. A.; Fokin, V. V. Direct Evidence of a Dinuclear Copper Intermediate in Cu(I)-Catalyzed Azide-Alkyne Cycloadditions. *Science* **2013**, *340*, 457−460.
(12) Özen, C.; Tüzün, N. Ş The Mechanism of Copper-Catalyzed Azide-Alkyne Cycloaddition Reaction: A Quantum Mechanical Investigation. *J. Mol. Graph. Model.* **2012**, *34*, 101−107.
(13) Chen, H.; Cai, C.; Li, S.; Ma, Y.; Luozhong, S.; Zhu, Z. Intermediates Stabilized by Tris(triazolylmethyl)amines in the CuAAC Reaction. *Chem.—Eur. J.* **2017**, *23*, 4730−4735.
(14) Venderbosch, B.; Oudsen, J.-P. H.; Van Der Vlugt, J. I.; Korstanje, T. J.; Tromp, M. Cationic Copper Iminophosphorane Complexes as CuAAC Catalysts: A Mechanistic Study. *Organometallics* **2020**, *39*, 3480−3489.
(15) Calvo-Losada, S.; Pino, M. S.; Quirante, J. J. On the regioselectivity of the mononuclear copper-catalyzed cycloaddition of azide and alkynes (CuAAC). A quantum chemical topological study. *J. Mol. Model.* **2014**, *20*, 2187.
(16) Calvo-Losada, S.; Pino, M. S.; Quirante, J. J. Rationalizing the Catalytic Activity of Copper in the Cycloaddition of Azide and Alkynes (CuAAC) with the Topology of $\nabla^2 \rho$ (r) and $\nabla \nabla^2 \rho$ (r). *J. Phys. Chem. B* **2015**, *119*, 1243−1258.
(17) Àvila, E. P.; de Oliveira, L. A.; Neto, B. A. D.; de Almeida, M. V.; Pliego, J. R., Jr. Flavanone-enabled CuAAC Reaction: Non-innocent Reagents Driving a Mononuclear Mechanism Over the Dinuclear Paradigm. *Chem.—Eur. J.* **2025**, *31*, 1−16.
(18) Kraka, E.; Antonio, J. J.; Freindorf, M. Reaction mechanism - explored with the unified reaction valley approach. *Chem. Commun.* **2023**, *59*, 7151−7290.
(19) Kraka, E.; Zou, W.; Tao, Y.; Freindorf, M. Exploring the Mechanism of Catalysis with the Unified Reaction Valley Approach (URVA) - A Review. *Catalysts* **2020**, *10*, 691.
(20) Kraka, E.; Quintano, M.; La Force, H. W.; Antonio, J. J.; Freindorf, M. The Local Vibrational Mode Theory and Its Place in the Vibrational Spectroscopy Arena. *J. Phys. Chem. A* **2022**, *126*, 8781−8798.
(21) Kraka, E.; Zou, W.; Tao, Y. Decoding Chemical Information from Vibrational Spectroscopy Data: Local Vibrational Mode Theory. *WIREs: Comput. Mol. Sci.* **2020**, *10*, 1480.
(22) Wilson, E. B.; Decius, J. C.; Cross, P. C. *Molecular Vibrations*; McGraw-Hill, New York, 1955.
(23) Wilson, E. B.; Decius, J. C.; Cross, P. C. *Molecular Vibrations. The Theory of Infrared and Raman Vibrational Spectra*; McGraw-Hill: New York, 1955.
(24) Konkoli, Z.; Cremer, D. A New Way of Analyzing Vibrational Spectra. I. Derivation of Adiabatic Internal Modes. *Int. J. Quantum Chem.* **1998**, *67*, 1−9.
(25) Konkoli, Z.; Larsson, J. A.; Cremer, D. A New Way of Analyzing Vibrational Spectra. II. Comparison of Internal Mode Frequencies. *Int. J. Quantum Chem.* **1998**, *67*, 11−27.
(26) Cremer, D.; Pople, J. A. General Definition of Ring Puckering Coordinates. *J. Am. Chem. Soc.* **1975**, *97*, 1354−1358.
(27) Madushanka, A.; Moura, R. T., Jr.; Verma, N.; Kraka, E. Quantum Mechanical Assessment of Protein-Ligand Hydrogen Bond Strength Patterns: Insights from Semiempirical Tight-Binding and Local Vibrational Mode Theory. *Int. J. Mol. Sci.* **2023**, *24*, 6311.
(28) Zou, W.; Freindorf, M.; Oliveira, V.; Tao, Y.; Kraka, E. Weak and strong π interactions between two monomers - assessed with local vibrational mode theory. *Can. J. Chem.* **2023**, *101*, 615−632.
(29) Peluzo, B. M. T. C.; Makoś, M. Z.; Moura, R. T., Jr.; Freindorf, M.; Kraka, E. Linear versus Bent Uranium(II) Metallocenes − A Local Vibrational Mode Study. *Inorg. Chem.* **2023**, *62*, 12510−12524.
(30) Quintano, M.; Moura, R. T., Jr.; Kraka, E. The pK_a rule in light of local mode force constants. *Chem. Phys. Lett.* **2023**, *826*, 140654.
(31) Peluzo, B. M.; Bodo, F.; Aeindartehran, L.; Runčevski, T.; Kraka, E. Thiabendazole: Fumaric acid as a case study on the salt cocrystal continuum: A local vibrational mode perspective. *Chem. Phys. Lett.* **2025**, *860*, 141772.
(32) Madushanka, A.; Laird, E.; Clark, C.; Kraka, E. SmartCADD: AI-QM Empowered Drug Discovery Platform with Explainability. *J. Chem. Inf. Model.* **2024**, *64*, 6799−6813.
(33) Madushanka, A.; Moura, R. T., Jr; Kraka, E. QM40, Realistic Quantum Mechanical Dataset for Machine Learning in Molecular Science. *Nature Scientific Data* **2024**, *11*, 1376.
(34) Antonio, J. J.; Kraka, E. Metal-ligand bonding and noncovalent interactions of mutated myoglobin proteins: a quantum mechanical study. *Pure Appl. Chem.* **2025**, *97*, 1435−453.
(35) Freindorf, M.; Kraka, E. Interplay between Metal Ligand Bonds and Hydrogen Bonds in Active Sites of Metal Substituted Myoglobins. *Dalton Trans.* **2025**, *54*, 4096−4111.
(36) Freindorf, M.; Fleming, K.; Kraka, E. Iron-histidine Coordination in Cytochrome b5: A Local Vibrational Mode Study. *ChemPhysChem* **2025**, *26*, e202401098.
(37) Freindorf, M.; Kraka, E. A Closer Look at the FeS Heme Bonds in *Azatobacter vinelandii Bacterioferritin*. *J. Comput. Chem.* **2025**, *46*, e70012.
(38) Bodo, F.; Erba, A.; Kraka, E.; Moura, R. T., Jr. Chemical Bonding in Uranium-based Materials: A Local Vibrational Mode Case Study of $Cs_2UO_2Cl_4$ and UCl_4 Crystals. *J. Comput. Chem.* **2024**, *45*, 1130−1142.
(39) Peluzo, B. M. T. C.; Moura, R. T., Jr.; Kraka, E. Extraction of uranyl from spent nuclear fuel wastewater via complexation - a local vibrational mode study. *J. Mol. Model.* **2024**, *30*, 126.
(40) Filatov Gulak, M.; Paolino, M.; Kaliakin, D.; Olivucci, M.; Kraka, E.; Min, S. K. Impact of solvation on the photoisomerisation dynamics of a photon- only rotary molecular motor. *Commun. Phys.* **2024**, *7*, 219.
(41) Neto, A. N. C.; Moura, R. T., Jr.; Carlos, L. D.; Malta, O. L.; Sanadar, M.; Melchior, A.; Kraka, E.; Ruggieri, S.; Bettinelli, M.; Piccinelli, F. Dynamics of the Energy Transfer Process in Eu(III) Complexes Containing Polydentate Ligands Based on Pyridine, Quinoline, and Isoquinoline as Chromophoric Antennae. *Inorg. Chem.* **2022**, *61*, 16333−16346.
(42) Moura, R. T., Jr.; Quintano, M.; Santos-Jr, C. V.; Albuquerque, V. A.; Aguiar, E. C.; Kraka, E.; Carneiro Neto, A. N. Featuring a new computational protocol for the estimation of intensity and overall quantum yield in lanthanide chelates with applications to Eu(III) mercapto-triazole Schiff base ligands. *Optical Materials: X* **2022**, *16*, 100216.
(43) Peluzo, B. M. T. C.; Moura, R. T., Jr.; Kraka, E. Conformation and Bonding of Lanthanide(III) Trihalides LnX_3 (Ln = La-Lu; X = F, Cl, Br): A Relativistic Local Vibrational Mode Study. *Inorg. Chem.* **2024**, *63*, 22445−22463.
(44) Machado, F. C.; Quintano, M.; Santos, C. V., Jr.; Neto, A. N. C.; Kraka, E.; Longo, R. L.; Moura, R. T., Jr. Theoretical insights into the vibrational spectra and chemical bonding of Ln(III) complexes with a tripodal N_4O_3 ligand along the lanthanide series. *Phys. Chem. Chem. Phys.* **2025**, *27*, 1794−1803.
(45) Saraiva, L. F.; Neto, A. N. C.; Bispo, A. G., Jr.; Quintano, M. M.; Kraka, E.; Carlos, L. D.; Lima, S. A. M.; Pires, A. M.; Moura, R. T., Jr. The role of vibronic coupling for the dynamics of intersystem crossing in Eu^{3+} complexes: An avenue for brighter compounds. *J. Chem. Theory Comput.h* **2025**, *21*, 3066−3076.
(46) Kelley, J. D.; Leventhal, J. J. *Problems in Classical and Quantum Mechanics: Normal Modes and Coordinates*; Springer, 2017; pp 95−117.
(47) Barone, V.; Alessandrini, S.; Biczysko, M.; Cheeseman, J. R.; Clary, D. C.; McCoy, A. B.; DiRisio, R. J.; Neese, F.; Melosso, M.; Puzzarini, C. Computational molecular spectroscopy. *Nat Rev Methods Primers* **2021**, *1*, 38.
(48) Zou, W.; Cremer, D. Properties of Local Vibrational Modes: The Infrared Intensity. *Theor. Chem. Acc.* **2014**, *133*, 1451−1466.
(49) Verma, N.; Tao, Y.; Zou, W.; Chen, X.; Chen, X.; Freindorf, M.; Kraka, E. A Critical Evaluation of Vibrational Stark Effect (VSE)

https://doi.org/10.1021/acs.jpca.6c00548
J. Phys. Chem. A 2026, 130, 4850−4864

Probes with the Local Vibrational Mode Theory. *Sensors* **2020**, *20*, 2358.
(50) Zou, W.; Kalescky, R.; Kraka, E.; Cremer, D. Relating Normal Vibrational Modes to Local Vibrational Modes with the Help of an Adiabatic Connection Scheme. *J. Chem. Phys.* **2012**, *137*, No. 084114.
(51) Moura, R. T., Jr.; Quintano, M.; Antonio, J. J.; Freindorf, M.; Kraka, E. Automatic Generation of Local Vibrational Mode Parameters: From Small to Large Molecules and QM/MM Systems. *J. Phys. Chem. A* **2022**, *126*, 9313−9331.
(52) Quintano, M.; Delgado, A. A. A.; Moura, R. T., Jr; Freindorf, M.; Kraka, E. Local mode analysis of characteristic vibrational coupling in nucleobases and Watson-Crick base pairs of DNA. *Electron. Struct.* **2022**, *4*, 044005.
(53) Quintano, M.; Moura, R. T., Jr.; Kraka, E. Frontier Article: Local vibrational mode theory meets graph theory: Complete and non-redundant local mode sets. *Chem. Phys. Lett.* **2024**, *849*, 141416.
(54) Saraiva, L. F.; Beltrame, A. C. F.; Bispo-Jr, A. G.; Canisares, F. S. M.; Neto, A. N. C.; Moura, R. T., Jr; Kraka, E.; Lima, S. A. M.; Pires, A. M. Unfolding the Photophysical Behavior of Luminescent Polymeric Films Containing β-Diketonate Tetrakis Eu^{III} Complexes via Multilayer Quantum Mechanics. *ACS Omega* **2025**, *10*, 30563−30575.
(55) Zou, W.; Cremer, D. C_2 in a Box: Determining its Intrinsic Bond Strength for the $X^1\Sigma^+_g$ Ground State. *Chem.—Eur. J.* **2016**, *22*, 4087−4099.
(56) Cremer, D.; Kraka, E. From Molecular Vibrations to Bonding, Chemical Reactions, and Reaction Mechanism. *Curr. Org. Chem.* **2010**, *14*, 1524−1560.
(57) Kraka, E.; Larsson, J. A.; Cremer, D. In *Computational Spectroscopy*; Grunenberg, J., Ed.; Wiley: New York, 2010; pp 105−149.
(58) Kalescky, R.; Kraka, E.; Cremer, D. Identification of the Strongest Bonds in Chemistry. *J. Phys. Chem. A* **2013**, *117*, 8981−8995.
(59) Mayer, I. C. bond order and valence in the ab initio theory. *Chem. Phys. Lett.* **1983**, *97*, 270−274.
(60) Mayer, I. Bond orders and valences from ab initio wave functions. *Int. J. Quantum Chem.* **1986**, *29*, 477−483.
(61) Mayer, I. Bond order and valence indices: A personal account. *J. Comput. Chem.* **2007**, *28*, 204−221.
(62) Kraka, E.; Freindorf, M. In *Topics in Organometallic Chemistry - New Directions in the Modeling of Organometallic Reactions*; Lledós, A., Ujaque, G., Eds.; Springer: Berlin, Heidelberg, 2020; Vol. *67*, pp 1−43.
(63) Marcus, R. A. Analytical mechanics of chemical reactions. 3. Natural collision coordinates. *J. Chem. Phys.* **1968**, *49*, 2610−2616.
(64) Hofacker, L. Quantentheorie Chemischer Reaktionen. *Z. Naturforsch. A* **1963**, *18*, 607−619.
(65) Kraka, E.; Dunning, T. H., Jr. In *Advances in Molecular Electronic Structure Theory: The Calculation and Characterization of Molecular Potential Energy Surfaces*; Dunning, T. H., Jr., Ed.; JAI Press, Inc.: Greenwich, 1990; pp 129−173.
(66) Dunning, T. H., Jr.; Harding, L. B., Kraka, E. *Supercomputer Algorithms for Reactivity, Dynamcis and Kinetics of Small Molecules*; Kluwer Academic Publishers, Dordrecht, Holland, 1989; p 57.
(67) Miller, W. H.; Handy, N. C.; Adams, J. E. Reaction path Hamiltonian for polyatomic molecules. *J. Chem. Phys.* **1980**, *72*, 99−112.
(68) Kato, S.; Morokuma, K. Potential energy characteristics and energy partitioning in chemical reactions: Ab initio MO study of four-centered elimination reaction $CH_3CH_2F \leftarrow CH_2 = CH_2 + HF$. *J. Chem. Phys.* **1980**, *73*, 3900−3914.
(69) Page, M.; McIver, J. W. On evaluating the reaction path Hamiltonian. *J. Chem. Phys.* **1988**, *88*, 922−935.
(70) Konkoli, Z.; Kraka, E.; Cremer, D. Unified Reaction Valley Approach Mechanism of the Reaction $CH_3 + H_2 \rightarrow CH_4 + H$. *J. Phys. Chem. A* **1997**, *101*, 1742−1757.
(71) Kühnel, W. *Differential Geometry: Curves - Surfaces - Manifolds*; American Mathematics Society, AMS: New York, 2005.
(72) Zou, W.; Sexton, T.; Kraka, E.; Freindorf, M.; Cremer, D. A New Method for Describing the Mechanism of a Chemical Reaction Based on the Unified Reaction Valley Approach. *J. Chem. Theory Comput.* **2016**, *12*, 650−663.
(73) Fleming, K.; Kraka, E. Examining Interstellar Ion-Neutral Reactions Using the Unified Reaction Valley Approach: The Case of the $CCl^+ + CH_3CN$ Reaction. *ACS Earth & Space Chem.* **2025**, *9*, 1837−1847.
(74) Freindorf, M.; Sexton, T.; Kraka, E.; Cremer, D. The Mechanism of the Cycloaddition Reaction of 1,3-Dipole Molecules with Acetylene - An Investigation with the Unified Reaction Valley Approach. *Theor. Chem. Acc.* **2014**, *133*, 1423.
(75) Becke, A. D.-e. T., III The Role of Exact Exchange. *J. Chem. Phys.* **1993**, *98*, 5648−5652.
(76) Lee, C.; Yang, W.; Parr, R. G. Development of the Colle-Salvetti Correlation-Energy Formula into a Functional of the Electron Density. *Phys. Rev. B* **1988**, *37*, 785−789.
(77) Dunning, T. H., Jr. Gaussian Basis Sets for Use in Correlated Molecular Calculations. I. The Atoms Boron Through Neon and Hydrogen. *J. Chem. Phys.* **1989**, *90*, 1007−1023.
(78) Fukui, K. The Path of Chemical Reactions — The IRC Approach. *Acc. Chem. Res.* **1981**, *14*, 363−368.
(79) Reed, A. E.; Curtiss, L. A.; Weinhold, F. Intermolecular Interactions from a Natural Bond Orbital, Donor-Acceptor Viewpoint. *Chem. Rev.* **1988**, *88*, 899−926.
(80) Weinhold, F.; Landis, C. R. *Valency and Bonding: A Natural Bond Orbital Donor-Acceptor Perspective*; Cambridge University Press, 2005.
(81) Weinhold, F.; Landis, C. R.; Glendening, E. D. What is NBO analysis and how is it useful? *Int. Rev. Phys. Chem.* **2016**, *35*, 399−440.
(82) Frisch, M. J.; Trucks, G. W.; Schlegel, H. B.; Scuseria, G. E.; Robb, M. A.; Cheeseman, J. R.; Scalmani, G.; Barone, V.; Petersson, G. A.; Nakatsuji, H.; Li, X.; Caricato, M.; Marenich, A. V.; Bloino, J.; Janesko, B. G.; Gomperts, R.; Mennucci, B.; Hratchian, H. P.; Ortiz, J. V.; Izmaylov, A. F.; Sonnenberg, J. L.; Williams-Young, D.; Ding, F.; Lipparini, F.; Egidi, F.; Goings, J.; Peng, B.; Petrone, A.; Henderson, T.; Ranasinghe, D.; Zakrzewski, V. G.; Gao, J.; Rega, N.; Zheng, G.; Liang, W.; Hada, M.; Ehara, M.; Toyota, K.; Fukuda, R.; Hasegawa, J.; Ishida, M.; Nakajima, T.; Honda, Y.; Kitao, O.; Nakai, H.; Vreven, T.; Throssell, K.; Montgomery, J. A., Jr.; Peralta, J. E.; Ogliaro, F.; Bearpark, M. J.; Heyd, J. J.; Brothers, E. N.; Kudin, K. N.; Staroverov, V. N.; Keith, T. A.; Kobayashi, R.; Normand, J.; Raghavachari, K.; Rendell, A. P.; Burant, J. C.; Iyengar, S. S.; Tomasi, J.; Cossi, M.; Millam, J. M.; Klene, M.; Adamo, C.; Cammi, R.; Ochterski, J. W.; Martin, R. L.; Morokuma, K.; Farkas, O.; Foresman, J. B.; Fox, D. J. *Gaussian 16*, Revision C.01; 2016; Gaussian Inc.: Wallingford CT.
(83) Tomasi, J.; Mennucci, B.; Cammi, R. Quantum Mechanical Continuum Solvation Methods. *Chem. Rev.* **2005**, *105*, 2999−3093.
(84) Neese, F. The ORCA Program System. *Wires* **2012**, *2*, 73−78.
(85) Liakos, D. G.; Guo, Y.; Neese, F. Comprehensive Benchmark Results for the Domain Based Local Pair Natural Orbital Coupled Cluster Method (DLPNO-CCSD(T)) for Closed- and Open-Shell Systems. *J. Phys. Chem.* **2020**, *124*, 90−100.
(86) Weigend, F.; Ahlrichs, R. Balanced basis sets of split valence, triple zeta valence and quadruple zeta valence quality for H to Rn: Design and assessment of accuracy. *Phys. Chem. Chem. Phys.* **2005**, *7*, 3297−3305.
(87) Kalescky, R.; Santos-Jr, C. V.; Tao, Y.; Zou, W.; Freindorf, M.; Cremer, D.; Kraka, E. *URVA2025*; Computational and Theoretical Chemistry Group (CATCO), Southern Methodist University: Dallas, TX, USA, 2025.
(88) Zou, W.; Moura, R., Jr.; Santos-Jr, C. V.; Quintano, M.; Bodo, F.; Freindorf, M.; Cremer, D.; Kraka, E. *LModeA*; Computational and Theoretical Chemistry Group (CATCO), Southern Methodist University: Dallas, TX, USA, 2025.
(89) Bader, R. F. W. A quantum theory of molecular structure and its applications. *Chem. Rev.* **1991**, *91*, 893−926.
(90) Bader, R. F. W. The Quantum Mechanical Basis of Conceptual Chemistry. *Monatshefte for Chemie* **2005**, *136*, 819−854.

https://doi.org/10.1021/acs.jpca.6c00548
J. Phys. Chem. A 2026, 130, 4850−4864

(91) Bader, R. F. W. *Atoms in Molecules: A Quantum Theory (International Series of Monographs on Chemistry)*; Clarendon Press, 1994.
(92) Keith, T. A. *AIMALL* (Version 19.10.12); 2019, URL: aim.tkgristmill.com; date of access: 04−10−2026.
(93) Cremer, D.; Kraka, E. Chemical Bonds without Bonding Electron Density? Does the Difference Electron-Density Analysis Suffice for a Description of the Chemical Bond? *Angew. Chem., Int. Ed.* **1984**, *23*, 627−628.
(94) Glendening, E. D.; Badenhoop, J. K.; Reed, A. E.; Carpenter, J. E.; Bohmann, J. A.; Morales, C. M.; Karafiloglou, P.; Landis, C. R.; Weinhold, F. *NBO 7.0. Theoretical Chemistry Institute*; University of Wisconsin: Madison, 2018.
(95) Cremer, D.; Kraka, E. Verification and Quantification of the Hammond-Leffler Postulate. *Rev. Proc. Quim.* **2012**, *6*, 27−30.
(96) Hammond, G. S. A Correlation of Reaction Rates. *J. Am. Chem. Soc.* **1955**, *77*, 334−338.

https://doi.org/10.1021/acs.jpca.6c00548
J. Phys. Chem. A 2026, 130, 4850−4864